

## Article

# Transient Behavior Analysis of Microgrids in Grid-Connected and Islanded Modes: A Comparative Study of LVRT and HVRT Capabilities

Abrar Shahriar Pramanik and Saeed Sepasi \*

Hawaii Natural Energy Institute, University of Hawaii at Manoa, Honolulu, HI 96822, USA;  
abrar@hawaii.edu

\* Correspondence: sepasi@hawaii.edu

**Abstract:** Microgrids, with integrated PV systems and nonlinear loads, have grown significantly in popularity in recent years, making the evaluation of their transient behaviors in grid-connected and islanded operations paramount. This study examines a microgrid's low-voltage ride-through (LVRT) and high-voltage ride-through (HVRT) capabilities in these operational scenarios. The microgrid's behavior was analyzed using both electromagnetic transient (EMT) and RMS simulation methods. Two operational modes, grid-connected and islanded, were considered. A three-phase diesel generator acted as a reference machine in islanded mode. Findings highlighted distinct behaviors in the two operational modes. The EMT simulation revealed in-depth characteristics of electrical parameters, showing high-frequency oscillations more precisely than the RMS simulation. Additionally, the transient recovery times were longer in islanded mode compared to grid-connected mode. The EMT simulation offers a more detailed portrayal of transient behaviors than the RMS simulation, especially in capturing high-frequency disturbances. However, its completion time becomes significantly extended with longer simulation durations. Microgrids showcase distinct transient behaviors in grid-connected versus islanded modes, especially in LVRT and HVRT scenarios. These findings are critical for the design and operation of modern microgrids.



**Citation:** Pramanik, A.S.; Sepasi, S. Transient Behavior Analysis of Microgrids in Grid-Connected and Islanded Modes: A Comparative Study of LVRT and HVRT Capabilities. *Clean Technol.* **2023**, *5*, 1287–1303. <https://doi.org/10.3390/cleantechnol5040065>

Academic Editors: Minas Patsalides and Venizelos Efthymiou

Received: 31 August 2023

Revised: 17 October 2023

Accepted: 7 November 2023

Published: 10 November 2023



**Copyright:** © 2023 by the authors. Licensee MDPI, Basel, Switzerland. This article is an open access article distributed under the terms and conditions of the Creative Commons Attribution (CC BY) license (<https://creativecommons.org/licenses/by/4.0/>).

**Keywords:** microgrid; LVRT; HVRT; EMT simulation; RMS simulation; PV

## 1. Introduction

In recent years, integrating renewable energy sources (RESes) into electrical power distribution networks has seen a significant surge. This spike is being driven mostly by legislative mandates aimed at reducing greenhouse gas (GHG) emissions from traditional electricity sources [1]. The incorporation of RESes has not only reduced the necessity for traditional electricity infrastructure expansion in many instances but also bolstered reliability and energy efficiency in power system distribution networks, due to localized generation and efficient demand-side control [2]. Consequently, vast financial resources have been allocated to research and enhance clean energy-generating techniques. This focus has positioned the renewable energy (RE) sector as the most dynamic and fast-growing segment within the energy industry, attracting an impressive USD 366 billion in investments in 2021 [3]. This global mobilization has created a foundation for a paradigm change and is fostering greater ambition among various organizations. As a result, RESes are significantly expanding worldwide, with a corresponding rise in their capacity and proportion of energy production.

RES covers a broad array of technologies, such as photovoltaic (PV) systems, wind turbines (WT), microturbines, and small-scale hydroelectric generators. These technologies are essential for building microgrids because of their adaptability and ability to integrate seamlessly into electrical networks with associated loads [4,5]. Moreover, energy storage

components like flywheels, batteries, and supercapacitors are commonly utilized within microgrids [5–7]. Microgrids operate in two primary modes. In islanded mode, they function as independent power systems, detached from the main distribution network [8–10], and in grid-connected mode, they stay connected to the main grid [11,12]. As the prevalence and scale of microgrids increase, several technical challenges arise. These challenges include (a) dynamic stability issues, (b) the coordination of protection schemes, and (c) concerns related to reliability and power quality (PQ) [1]. The dynamic stability issues of a grid-connected microgrid were studied and improved using the battery energy storage system (BESS) described in [13]. This work also focuses on the maximum power point tracking (MPPT) of the PV system and the control mechanism of the grid-side converter (GSC). Both utilize the adaptive neuro-fuzzy inference system (ANFIS) algorithm to ensure consistent voltage and frequency within the system. In [14], the authors introduced a modified protection coordination strategy for microgrids, taking into account user-specified dual-setting directional overcurrent relays (DS-DOCRs) that ensure coordination in both grid-connected and islanded modes. The primary goal of this research was to identify shared optimal relay settings, including the time multiplier setting (TMS), plug setting (PS), and relay characteristic constants ( $\alpha$ ), which ensure effective coordination during each mode. To address the PQ issues, a comprehensive review article in [15] presents an insight into PQ concerns in microgrids, discussing a range of PQ disruptions, their primary characteristics, and pertinent PQ standards. Moreover, it delves into a thorough review of existing case studies concerning PQ analysis in microgrids and systems powered by renewable energy. Among all the challenges mentioned above, dynamic stability has garnered significant attention. Dynamic stability concerns emerge when non-inverter-interfaced generators (like traditional generators) and inverter-interfaced renewable energy generators (such as PV systems) coexist within the microgrid. This highlights the pressing need to study dynamic phenomena in microgrids.

Dynamic phenomena in power systems are broadly categorized into electromagnetic and electromechanical phenomena, each operating on different time scales [16]. Electromagnetic phenomena are associated with transient electrical states, such as current flow dynamics through inductance, or voltage variations at capacitance. On the other hand, electromechanical phenomena mainly encompass the dynamics of synchronous machines' swing equations within the power system [16,17]. To analyze electromechanical phenomena, root mean square (RMS) simulations, also known as phasor simulations, are frequently utilized [18]. In these simulations, all lines and associated utilities are modeled using algebraic equations for a fixed frequency, disregarding the electrical states of the network [19]. RMS-based simulations are efficient for quickly assessing large systems, but they are constrained in their accuracy, representing only transients of the fundamental frequency or lower, making them unable to capture rapid converter dynamics. Electromagnetic transient (EMT) simulations are typically performed to investigate dynamic electromagnetic phenomena comprehensively. These simulations involve all electrical states and represent network equations using differential equations. The reactance values of capacitive and inductive elements change with frequency, and detailed models of electrical components and controllers are employed [20]. EMT simulations utilize time steps shorter than 50 microseconds, enabling them to capture the rapid dynamics in the power system caused by power electronic devices like voltage source converters (VSCs), commonly used as connectors between RESes and distribution grids [21]. However, the detailed representation and short time step required for EMT simulations imposes computational limitations, making them more feasible only for small-scale systems [22]. Table 1 represents the voltage across a resistor, an inductor, and current across a capacitor in both EMT and RMS simulation techniques.

**Table 1.** RMS and EMT simulation techniques.

Element	RMS	EMT
Resistor	$IR$	$IR$
Inductor	$Ij\omega L$	$L \frac{di}{dt}$
Capacitor	$Vj\omega C$	$C \frac{dV}{dt}$

Both RMS and EMT simulations are valuable tools for power system analyses. When examining converter protection, synchronization, or the interaction between converter control and network resonance, EMT simulation is the preferred choice. Apart from these, RMS still offers significant accuracy when assessing the effects of converters on power system operation. The RMS concept was basically developed to streamline the analysis of machine dynamics and dynamic loads. The utility of RMS might be questioned if the system lacks a sufficient number of machines, though defining “sufficient” is ambiguous in this context. Specifically, when converters predominantly dictate system dynamics, the relevance of RMS might diminish. A sample case is the network energization or black start via grid-forming control, which is not effectively studied using RMS. However, RMS simulations are more data-efficient than EMT models. While EMT simulations require comprehensive datasets, which are often challenging to obtain, RMS can operate with minimal data. So, selecting the right simulation approach is contingent upon the network’s characteristics, the study’s goals, and the trade-off between efficiency and accuracy. Moreover, the computer’s processing power and the challenge of obtaining data for EMT studies are also pivotal considerations.

A considerable volume of research is dedicated to both EMT and RMS simulations. Among them, analyzing the low-voltage ride-through (LVRT) and high-voltage ride-through (HVRT) capabilities are some of the most significant ones. LVRT and HVRT are the capabilities of electric generators to stay connected during low-voltage and high-voltage faults in the grid, respectively, and keep supporting the grid at this time [23]. In the evolving landscape of microgrid exploration and innovation, the roles of HVRT and LVRT are of paramount importance. Microgrids, characterized as localized energy systems, amalgamate a diverse array of both renewable and traditional energy sources. Given the inherent intermittency of renewable energy and the susceptibility to various external and internal disturbances, voltage perturbations are an anticipated challenge. The incorporation of HVRT and LVRT capabilities serves as a protective barrier against such voltage deviations, ensuring uninterrupted operation and mitigating the risk of unscheduled disconnections [24]. This becomes even more critical during instances when the microgrid is operating in an islanded mode, independent of the primary grid, where the responsibility for stability rests solely on the microgrid’s infrastructure [25]. Moreover, as microgrids increasingly cater to sensitive equipment and mission-critical loads, the protective shield offered by HVRT and LVRT becomes indispensable, safeguarding these integral components from potential harm arising from voltage anomalies. In [26], LVRT capability has been analyzed and compared between RMS and EMT models by introducing a short-circuit fault in the system [22]. In this work, the authors compared the responses of traditional generators and wind turbines using EMT simulations in PSCAD and RMS simulations in Digsilent. The comparison included multiple scenarios, such as load step changes and short-circuit faults. In [27], intentional islanding within a microgrid was studied through three distinct case scenarios: (1) The microgrid was powered only by rotating generators, (2) The microgrid was powered only by static generators, and (3) A combination of both types of generators powered the microgrid. The LVRT capabilities of the generators were analyzed and compared between the mentioned scenarios while disconnecting the microgrid from the main grid. Voltage, frequency, and active and reactive power variations were the main focus of this work. RMS simulation was utilized to conduct this research in Digsilent software 2022. In [28], the LVRT capability of the PV system during fault was analyzed. The authors of that study also analyzed the model response

when PV generation dropped. Additionally, ref. [29] presented a comparative analysis of an Australian 14-generator test system with advanced energy-conversion systems (ACESes), introducing a three-phase to ground fault using RMS and EMT simulations. Given the computational demands associated with EMT simulations, the authors used real-time simulation (RSCAD/RTDS) for the real-time digital simulator (RTS) model, and the RMS modeling was performed in PSS/E software 2017. In [30], an adaptive virtual inertia control strategy was proposed to analyze the LVRT and HVRT capabilities of a solar system through dynamic simulations. In [23], the HVRT capability of a fully rated converter-based wind turbine was analyzed using EMT simulation in Digsilent software 2021. Moreover, the HVRT and LVRT capability of a PV system was conducted and analyzed in [31]. They used the hardware in the loop (HIL) platform for this research. Overall, these studies aimed to enhance the understanding of power system behavior under various conditions and used EMT and RMS simulations in different scenarios to analyze their case studies. In this study, we introduced a unique case scenario. We examined the impact of a significant nonlinear load, two PV systems, and a backup diesel generator within a microgrid. Their behaviors were analyzed and contrasted during both grid-connected and islanded operations using EMT and RMS simulation methodologies.

This research presents the dynamic response analysis of a microgrid for different scenarios in both grid-connected and islanded modes with the presence of PV systems, a nonlinear load, and a backup diesel generator. The generator starts working only when the microgrid is in islanded mode. This study utilizes an adapted Digsilent microgrid model with necessary modifications to ensure relevance. All simulations for this work were executed using the Digsilent software 2022. The main contributions of this paper are to compare the responses of two dynamic models (EMT and RMS) in two case scenarios: (1) Analyzing the microgrid's LVRT capabilities, (2) Evaluating the high-voltage ride-through (HVRT) capabilities. These analyses are conducted in both grid-connected and islanded modes. The remaining sections of this paper are organized as follows. A description of the microgrid model with details of all the components is presented in Section 2. In Section 3, the results are analyzed, and the comparisons between EMT and RMS simulations are discussed. The summary and conclusions are set out in Section 4.

## 2. Microgrid Model Description

The base model of the microgrid for this research is taken from an inbuilt Digsilent/PowerFactory model [32]. Some modifications were made for the sake of the suitability of this research. In the in-built design, there was no PV system and no nonlinear load. These components were added for this research. Moreover, we reduced the number of generators from three to one and used that generator as a backup reference machine in islanded mode. Additionally, we modified the loads, lines, and transformer parameters, and made the microgrid system a low-voltage system of 0.48 kV from 20 kV. This AC microgrid operates at a nominal frequency of 60 Hz. The grid-side nominal voltage is 12.47 kV, while the distribution side operates at 0.48 kV (line-to-line). Figure 1 presents a one-line diagram of this modified microgrid model. A detailed description of each component within the microgrid is provided in the following subsections.

### 2.1. Lines

This microgrid model incorporates sixteen distinct lines, each varying in length. Several critical parameters, including resistance, reactance, and susceptance, are considered for line modeling. For this study, the values of these parameters are chosen for 20 °C.

These parameters are dependent on the characteristics of the cable. There are two types of cable used in this model. Both are chosen from the Digsilent library [33], and the parameters are modified where needed. All the cables are three-phase underground-type cables with aluminum used as conductor material. The maximum operating temperature is 80 °C. The parameters of the cables are shown in Table 2.

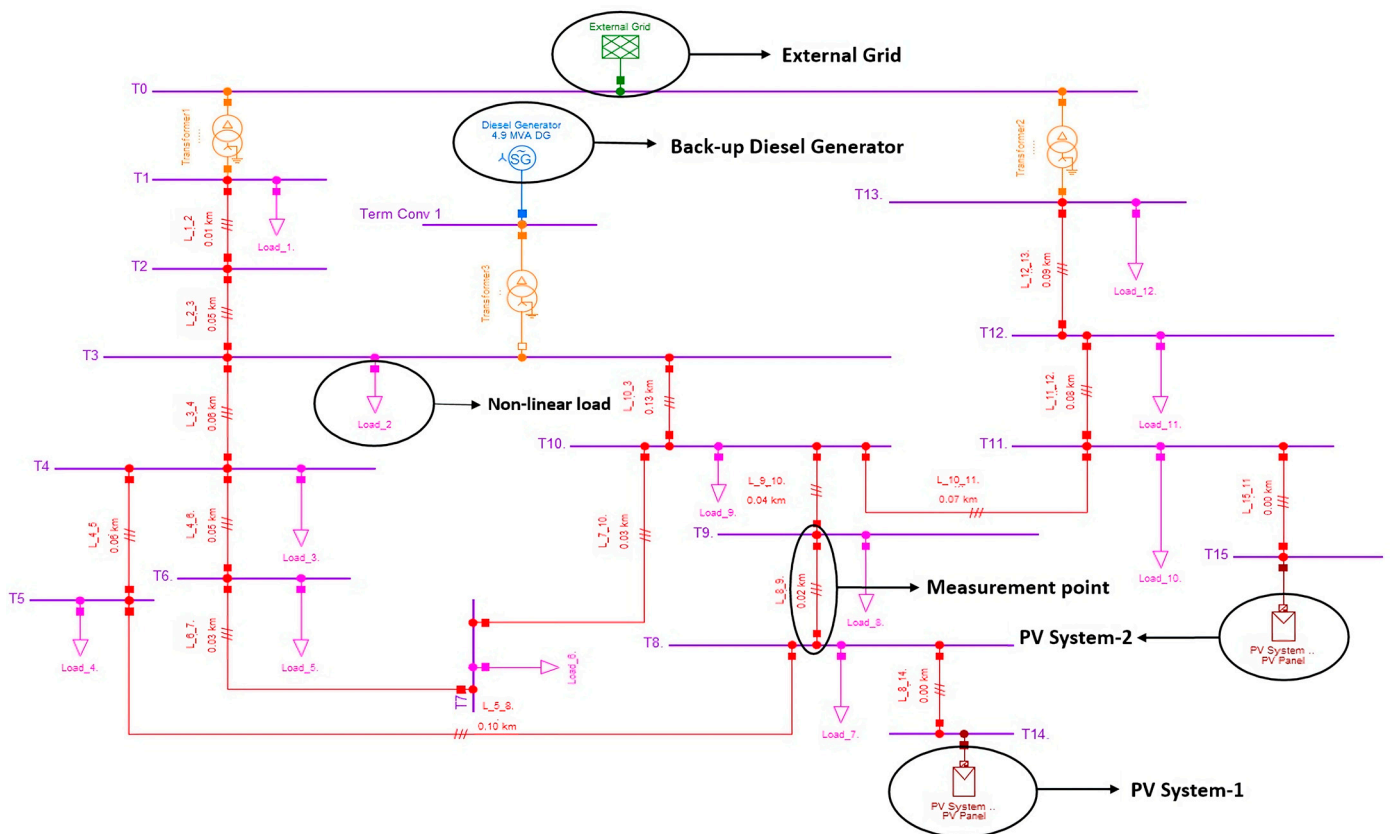


Figure 1. Single-line diagram of the modified microgrid.

Table 2. Line parameters.

Cable	Length (km)	Resistance-1,2 Sequence (Ohm/km)	Resistance-0 Sequence (Ohm/km)	Reactance-1,2 Sequence (Ohm/km)	Reactance-0 Sequence (Ohm/km)	Susceptance-1,2 Sequence ( $\mu S/km$ )	Susceptance-0 Sequence ( $\mu S/km$ )	Rated Voltage (kV)	Rated Current (kA)
Line 1_2	0.01	0.501	0.817	0.716	1.598	47.493	37.994	0.48	1
Line 2_3	0.045	0.501	0.817	0.716	1.598	47.493	37.994	0.48	1
Line 3_4	0.061	0.501	0.817	0.716	1.598	47.493	37.994	0.48	1
Line 4_5	0.056	0.501	0.817	0.716	1.598	47.493	37.994	0.48	1
Line 4_6	0.045	0.501	0.817	0.716	1.598	47.493	37.994	0.48	1
Line 5_8	0.10	0.501	0.817	0.716	1.598	47.493	37.994	0.48	1
Line 6_7	0.033	0.501	0.817	0.716	1.598	47.493	37.994	0.48	1
Line 7_10	0.032	0.501	0.817	0.716	1.598	47.493	37.994	0.48	1
Line 8_9	0.024	0.501	0.817	0.716	1.598	47.493	37.994	0.48	1
Line 8_14	0.002	0.501	0.817	0.716	1.598	47.493	37.994	0.48	1
Line 9_10	0.04	0.501	0.817	0.716	1.598	47.493	37.994	0.48	1
Line 10_3	0.13	0.501	0.817	0.716	1.598	47.493	37.994	0.48	1
Line 15_11	0.002	0.501	0.817	0.716	1.598	47.493	37.994	0.48	1
Line 10_11	0.07	0.51	0.658	0.366	1.611	3.172	1.28	0.48	1
Line 11_12	0.08	0.51	0.658	0.366	1.611	3.172	1.28	0.48	1
Line 12_13	0.09	0.51	0.658	0.366	1.611	3.172	1.28	0.48	1

### 2.2. Loads

In this study, except Load<sub>2</sub>, all loads are balanced and linear. This load is designed as a nonlinear load to observe the effect of a sizeable nonlinear load during dynamic simulations. These loads are characterized as ‘3Phase-D’ types [34]. Figure 2 shows this type of load’s configuration.

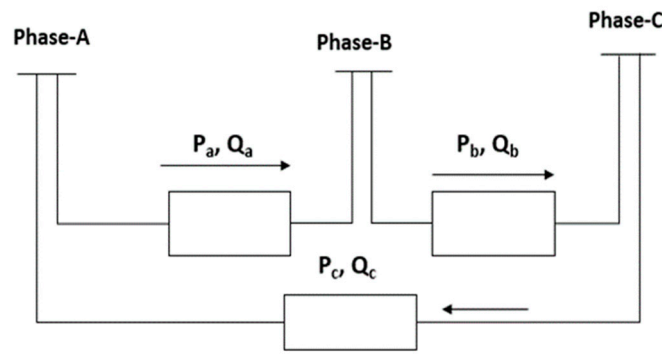


Figure 2. ‘3Phase-D’ load model.

Three polynomial terms are used to model the load model’s voltage dependency, as outlined in equations 1 and 2 [34]. Here,  $P_a, P_b, P_c, Q_a, Q_b,$  and  $Q_c$  represent the proportional coefficients, while  $e_{P_a}, e_{P_b}, e_{P_c}, e_{Q_a}, e_{Q_b},$  and  $e_{Q_c}$  are the corresponding exponents. The term  $u_0$  is the input voltage parameter, and  $|u|$  stands for the absolute voltage at the connection point of the load. Various exponential and polynomial models can be defined by choosing different proportional and exponential coefficient values. Constant power, constant current, and constant impedance type load models can be defined by modifying the exponential coefficients to 0, 1, and 2, respectively. In this research, a constant impedance model is used for all loads. Additional key parameters used in this research are listed in Table 3.

$$P = P_0 \cdot \left[ P_a \cdot \left( \frac{|u|}{u_0} \right)^{e_{P_a}} + P_b \cdot \left( \frac{|u|}{u_0} \right)^{e_{P_b}} + (1 - P_a - P_b) \cdot \left( \frac{|u|}{u_0} \right)^{e_{P_c}} \right] \tag{1}$$

$$Q = Q_0 \cdot \left[ Q_a \cdot \left( \frac{|u|}{u_0} \right)^{e_{Q_a}} + Q_b \cdot \left( \frac{|u|}{u_0} \right)^{e_{Q_b}} + (1 - Q_a - Q_b) \cdot \left( \frac{|u|}{u_0} \right)^{e_{Q_c}} \right] \tag{2}$$

Table 3. Load parameters.

Load	Apparent Power (kVA)	Active Power (kW)	Reactive Power (kVar)	Power Factor
Load <sub>1</sub>	200	190	62.44	0.95
Load <sub>2</sub> (nonlinear load)	122	100	38.08	0.82
Load <sub>3</sub>	50	47.5	15.61	0.95
Load <sub>4</sub>	70	66.5	21.86	0.95
Load <sub>5</sub>	35	33.25	10.93	0.95
Load <sub>6</sub>	80	76	24.98	0.95
Load <sub>7</sub>	45	42.75	14.05	0.95
Load <sub>8</sub>	13	12.35	4.06	0.95
Load <sub>9</sub>	72	68.40	22.48	0.95
Load <sub>10</sub>	55	52.25	17.17	0.95
Load <sub>11</sub>	5	4.75	1.56	0.95
Load <sub>12</sub>	75	71.25	23.42	0.95

As outlined in Table 2, the total apparent power of the microgrid’s loads is 822 KVA. Among all these loads, Load<sub>2</sub> is nonlinear. The nonlinearity of the load comes from injecting harmonic currents into it. The load is designed so that the total harmonic distortion (THD) of the load is 29.4%.

### 2.3. Transformers

Three ‘3Phase-2 windings’ transformers are used in this study [35]. Table 4 provides key specifications and characteristics of these transformers.

**Table 4.** Transformer parameters.

Names	Positive Sequence Impedance-Reactance/Resistance (p.u.)	Zero Sequence Impedance-Reactance/Resistance (p.u.)	Rated Power (KVA)	Rated Voltage-HV/LV (kV)	Vector Group HV/LV	Copper Losses (kW)	Nominal Frequency (Hz)
Transformer-1	0.0618/0.0106	0.0494/0.0851	2500	12.47/0.48	D/YN	26.5	60
Transformer-2	0.0618/0.0106	0.0494/0.0851	2500	12.47/0.48	D/YN	26.5	60
Transformer-3	0.0599/0.0014	0.04792/0.0011	2000	10.5/0.48	D/YN	2	60

2.4. Busbars

In this microgrid’s distribution system, all busbars operate at 0.48 kV, except for those near the grid and the diesel generator, which operate at 12.47 kV and 10.5 kV, respectively. All busbars in the system are based on 3-phase technology.

2.5. PV System

PV systems can be modeled in two ways: the ‘active power input mode’, which supplies active power, and the ‘solar calculation mode’, which adjusts power generation based on panel specs, array setup, time, and date. The active power input mode is preferred for short simulations like EMT and RMS analyses, spanning seconds to minutes. On the other hand, the solar calculation mode is more suitable for longer simulations covering a day or more. In this study, the active power input mode was employed to model two PV systems, and the standard PV system dynamic model from Digsilent software 2022 was adapted and modified to fit the research requirements. The modified dynamic model of the PV system is depicted in Figure 3. Each component of the model is described as follows.

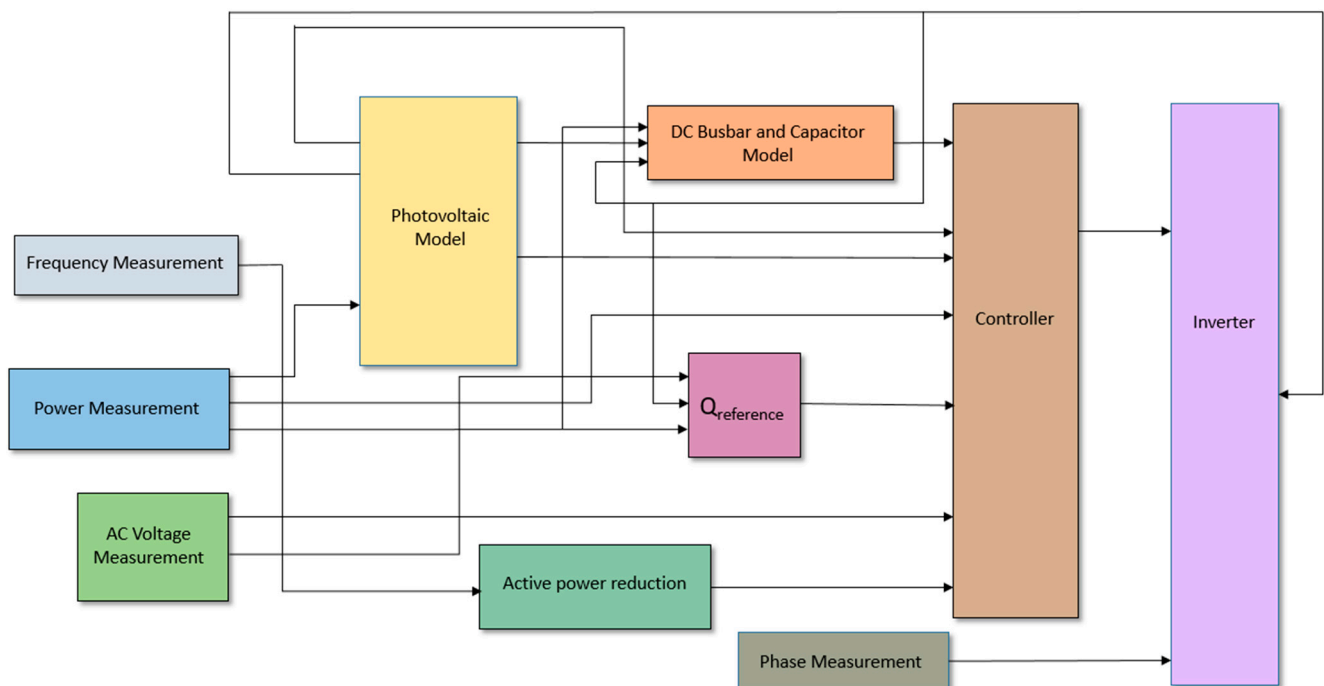


**Figure 3.** Dynamic model of PV systems.

2.5.1. Photovoltaic Model

In the photovoltaic model of the PV system, the parameters regarding the PV panels are defined. The model is implemented using Digsilent Simulation Language (DSL) [33]. The details of these parameters can be found in Table 5.

**Table 5.** Photovoltaic model parameters.

Parameter	Values
Open-circuit voltage of module at STC (V)	43.8
MPP voltage of module at STC (V)	35
MPP current of module at STC (A)	4.58
Short-circuit current of module at STC (A)	5
Number of modules in series	20
Over-sizing factor for PV plant	1

### 2.5.2. Power Measurement

A power measurement block determines power flow at any element connected to a busbar. For this study, a three-phase power measurement element is utilized for this purpose. Its output is connected with various other elements, such as the PV, controller,  $Q_{\text{reference}}$ , and DC busbar and capacitor models. Power output signals are calculated using Equations (3) and (4) during the ‘balanced RMS’ simulation.

$$p = \text{Re}\{3 \cdot u_1 \cdot i_1^*\} \quad (3)$$

$$q = \text{Im}\{3 \cdot u_1 \cdot i_1^*\} \quad (4)$$

where  $p$  and  $q$  represent the real and reactive power, respectively;  $u_1$  and  $i_1$  are complex voltages and currents measured from RMS balanced simulation; and  $*$  is the complex conjugate operator [36].

Equations (5)–(10) are employed for ‘unbalanced RMS’ operations:

$$p_1 = \text{Re}\left\{\sqrt{2} \cdot 3 \cdot u_1 \cdot i_1^*\right\} \quad (5)$$

$$q_1 = \text{Im}\left\{\sqrt{2} \cdot 3 \cdot u_1 \cdot i_1^*\right\} \quad (6)$$

$$p_0 = \text{Re}\left\{\sqrt{2} \cdot 3 \cdot u_0 \cdot i_0^*\right\} \quad (7)$$

$$q_0 = \text{Im}\left\{\sqrt{2} \cdot 3 \cdot u_0 \cdot i_0^*\right\} \quad (8)$$

$$p_2 = \text{Re}\left\{\sqrt{2} \cdot 3 \cdot u_2 \cdot i_2^*\right\} \quad (9)$$

$$q_2 = \text{Im}\left\{\sqrt{2} \cdot 3 \cdot u_2 \cdot i_2^*\right\} \quad (10)$$

where  $p_1, q_1$  represent positive sequence output active, and reactive power  $p_0, q_0$  are the zero sequence, and  $p_2, q_2$  are the negative sequence active and reactive output power [36].

In 3-phase EMT simulations, phase voltage and current are transformed using the  $\alpha\beta\gamma$  transformation. To obtain the corresponding  $\alpha\beta\gamma$  components. The active and reactive power outputs are computed using Equations (11)–(13).

$$p = \text{Re}\left\{\frac{3}{2} \cdot (u_\alpha + ju_\beta) \cdot (i_\alpha - ji_\beta)\right\} \quad (11)$$

$$q = \text{Im}\left\{\frac{3}{2} \cdot (u_\alpha + ju_\beta) \cdot (i_\alpha - ji_\beta)\right\} \quad (12)$$

$$p_0 = \frac{3}{2} \cdot u_\gamma \cdot i_\gamma \quad (13)$$

where  $u_\alpha$ ,  $u_\beta$ , and  $u_\gamma$  represent the voltages and currents from the  $\alpha\beta\gamma$  transformation, while  $i_\alpha$ ,  $i_\beta$ , and  $i_\gamma$  show the corresponding currents [36]. The outputs of the  $\alpha$  and  $\beta$  components are represented by  $p$  and  $q$ , respectively, and the output of the  $\gamma$  component is denoted as  $p_0$ .

### 2.5.3. A.C. Voltage Measurement

A three-phase voltage measurement device measures the terminal voltages in this study. Its output interfaces with both the controller and  $Q_{\text{reference}}$ . Typically, voltage magnitudes are derived from the real and imaginary components of the corresponding voltage, as described by Equation (14) [37]:

$$u = \sqrt{ur^2 + ui^2} \quad (14)$$

In 3-phase RMS simulations, the output voltages are calculated using Equations (15)–(17) [37]:

$$V_1 = u_1r + ju_1i = \frac{1}{3} \cdot \left( u_a + \left( -\frac{1}{2} + j\frac{\sqrt{3}}{2} \right) \cdot u_b + \left( -\frac{1}{2} - j\frac{\sqrt{3}}{2} \right) \cdot u_c \right) \quad (15)$$

$$V_0 = u_0r + ju_0i = \frac{1}{3} \cdot (u_a + u_b + u_c) \quad (16)$$

$$V_2 = u_2r + ju_2i = \frac{1}{3} \cdot \left( u_a + \left( -\frac{1}{2} + j\frac{\sqrt{3}}{2} \right) \cdot u_b + \left( -\frac{1}{2} - j\frac{\sqrt{3}}{2} \right) \cdot u_c \right) \quad (17)$$

where  $V_1$ ,  $V_2$ , and  $V_0$  are the positive, zero, and negative sequence measured voltages, respectively. Furthermore,  $u_a$ ,  $u_b$ , and  $u_c$  correspond to the voltages of phases a, b, and c.

For 3-phase EMT analysis, output voltages are derived using Equations (18)–(20) [37]:

$$ur = u_\alpha = \frac{1}{3} \cdot (2 \cdot u_a - u_b - u_c) \quad (18)$$

$$ui = u_\beta = \frac{1}{3} \cdot (\sqrt{3} \cdot u_b - \sqrt{3} \cdot u_c) \quad (19)$$

$$u_0 = u_\gamma = \frac{1}{3} \cdot (u_a + u_b + u_c) \quad (20)$$

These computations involve the  $\alpha\beta\gamma$  transformation, where  $ur$ ,  $ui$ , and  $u_0$  are the representatives of  $\alpha$ ,  $\beta$ , and  $\gamma$  components, respectively.

### 2.5.4. Phase Measurement

A phase-locked loop (PLL) is employed to ascertain the frequency and phase of system voltage. While three models are available in Digsilent software 2022 for PLL, Version 1, Version 2, and Version 3, this research exclusively utilizes PLL model Version 3. Comprehensive details, including block diagrams, computational parameters, and the functionality of Version 3 for both RMS and EMT simulations, can be found in [38].

### 2.5.5. Frequency Measurement, Active Power Reduction, and DC Busbar and Capacitor Model

The PLL is additionally utilized for frequency measurement, albeit with slower settings. In case of over-frequency, a DSL model with power reduction logic is used, as outlined in [33,38]. The system is configured to initiate the power reduction device when the frequency increases to 60.2 Hz, operating at a 40% gradient. A DC link capacitor with a value of 35  $\mu\text{F}/\text{Kw}$  is incorporated into the model to serve as a coupling element.

### 2.5.6. $Q_{\text{reference}}$ and Controller

$Q_{\text{reference}}$  defines the control mode of the reactive power, while the central Controller oversees the overall DC voltage and limits on reactive power. These control units are also implemented using DSL models. Some of the significant parameters of the control units are shown in Table 6.

**Table 6.** Control parameters.

Name	Unit	Description	Value
Kp	-	Gain of active-power PI controller	0.005
Tr	s	Measurement delay	0.001
Tmpp	s	Time-delay MPP tracking	5
KFRT	-	Gain for dynamic AC voltage support	2
Kpq	-	Gain of reactive-power PI controller	0.1
Tpick	s	Pick-up time for fault detection	0.01
Ulvrt	p.u.	Voltage threshold for LVRT detection	0.95
Uhvrt	p.u.	Voltage threshold for HVRT detection	1.05
Tdyn_max	s	Max. duration fault mode	5
iq_min	p.u.	Minimum reactive current limit	-1
iq_max	p.u.	Maximum reactive current limit	1
Id_max	p.u.	Maximum active current limit	1

### 2.5.7. Inverter

A static generator is used for the representation of the inverter in the model. It allows for the definition of rated apparent power, operating active power, and rated power factor. For PV System-1, these are set at 450 KVA, 450 kW, and 1, respectively, while for PV System-2, they are 150 KVA, 150 kW, and 1. PV System-1 is considered the primary system due to its larger size. The rest of the equipment's configurations of the PV systems are the same for both systems. There are several local controllers available for the static generator. In this work, the constant Q controller is used [39]. This generator can be used as current source, voltage source, constant impedance, and constant power depending on the input signals it receives [39]. For this work, it is used as a current source, and it has two different current source models for two dynamic simulations, RMS and EMT [39].

### 2.6. Diesel Generator

Within the microgrid, a rotating diesel generator, paired with a governor and an automatic voltage regulator (AVR), acts as the reference machine during islanded operation simulations. In this mode, it connects through an automatic transfer switch (ATS). A 3-phase YN-connected synchronous machine serves this function, complemented by a control mechanism designed for dynamic simulations. Key parameters of this synchronous machine can be found in Table 7.

**Table 7.** Basic parameters of synchronous machine.

Title 1	Title 2
Rated apparent power (MW)	4.855
Rated voltage (kV)	10.5
Rated power factor	0.8
Connection	3-phase YN
Local controller type	Constant V [40]

For synchronous machines, several models are available for both RMS and EMT simulations, including (1) Standard, (2) Model 3.3, (3) Classical, and (4) Asynchronous starting. Each model possesses distinct calculation methods for EMT and RMS simulations [40]. In this study, the standard model is selected for the synchronous machine.

### 3. Results and Discussion

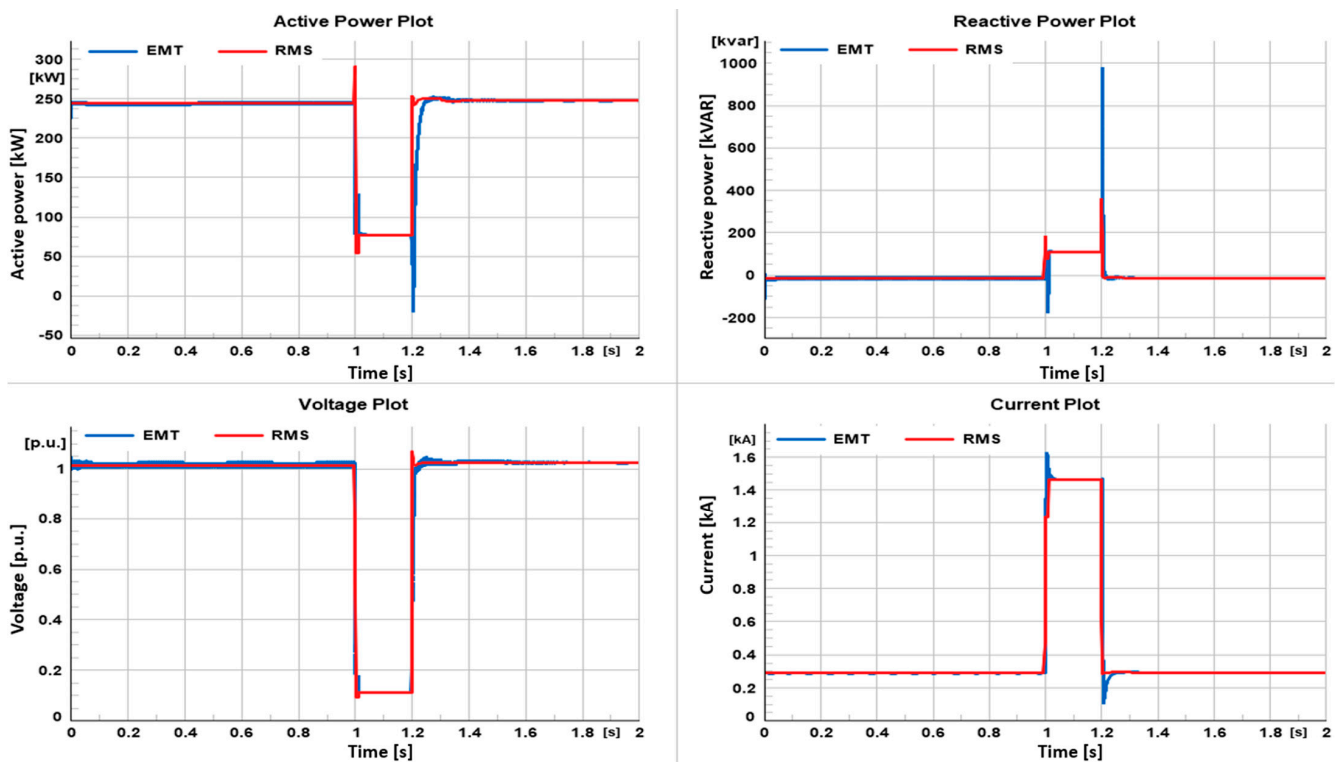
As described earlier, two case studies are considered for this work: (1) Grid-connected microgrid, and (2) Islanded microgrid. There are two PV systems presented in this microgrid in both case studies and a backup diesel generator, which works as a reference machine during the islanded mode but remains turned off while the microgrid is connected to the grid. The LVRT and HVRT capabilities of the system are analyzed in both cases using RMS and EMT simulation methods. Line\_8\_9 is the measured point for all analyses. This location is strategically chosen due to its position at the center of the significant components within the microgrid, such as the large nonlinear load, diesel generator, and the main PV system (PV system-1). Consequently, this point offers a clear vantage to observe the effects of these components on the microgrid, enhancing the effectiveness of the analyses conducted.

#### 3.1. Grid-Connected Mode

An external grid is connected to the microgrid for the analyses. The basic configuration of the external grid is taken from the Digsilent library and modified according to the study [41]. Both the LVRT and HVRT capabilities of the system are analyzed using RMS and EMT simulations.

##### 3.1.1. LVRT Case Scenario

For the LVRT analysis, a three-phase short-circuit fault was applied at the busbar (T9) connected to Line\_8\_9. The fault was initiated at the 1 s mark and lasted for 200 milliseconds in RMS and EMT simulations. The total simulation duration was set to 2 s for both methods. The step sizes were one millisecond for RMS and 0.01 milliseconds for EMT simulations. Figure 4 represents the characteristics of active power, reactive power, voltage, and current parameters during the three-phase short-circuit fault in grid-connected mode.



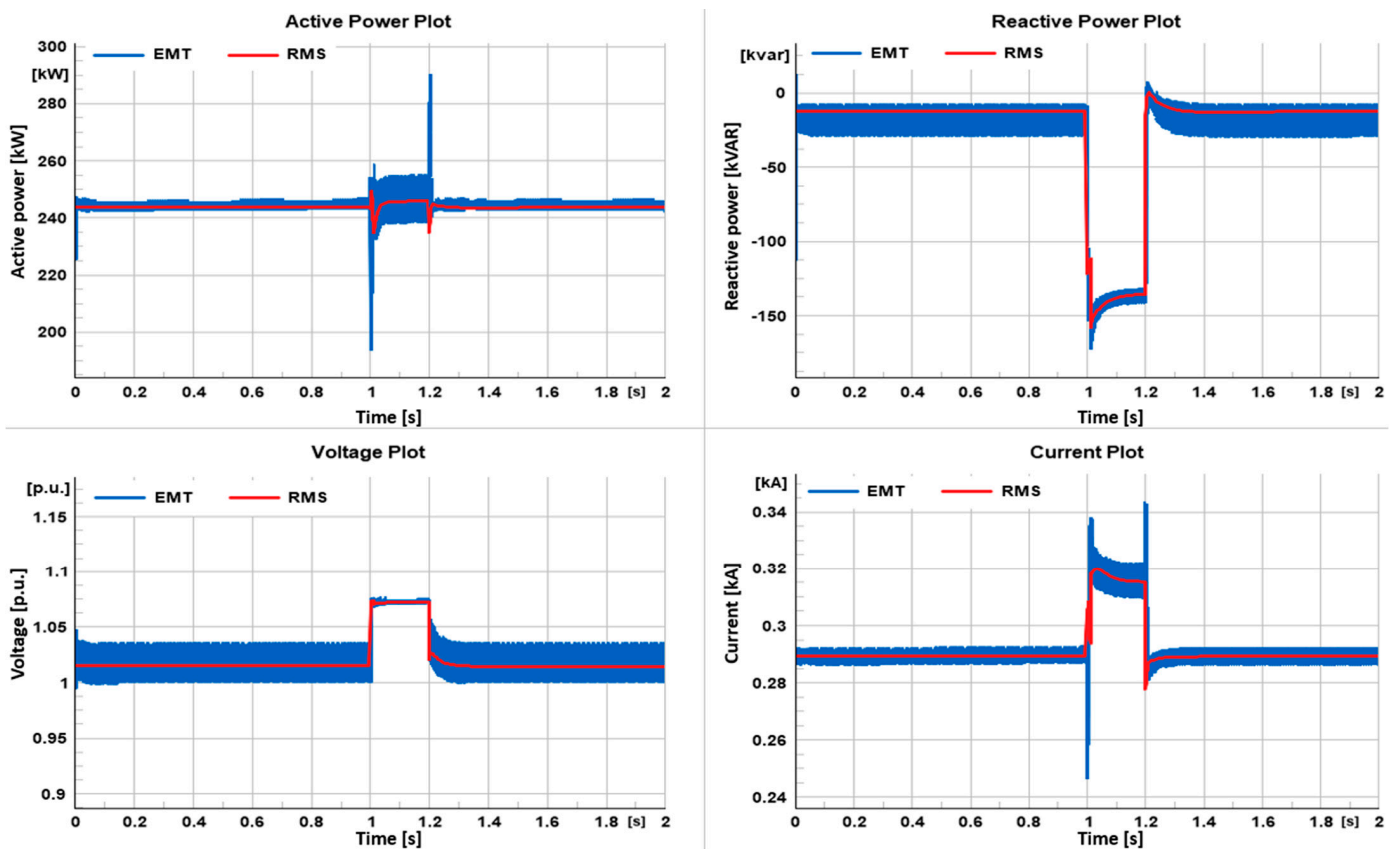
**Figure 4.** Active power, reactive power, voltage, and current behaviors during 3-phase short-circuit fault in grid-connected mode.

Figure 4 shows four key parameters for this analysis: active power, reactive power, voltage, and current. In each subplot, a discernible disturbance is evident from the 1 s mark extending to 1.2 s, which is attributable to the three-phase short-circuit fault. A magnified view of this disturbance is provided in a smaller inset within each subplot for a more detailed examination. These insights show that the PV systems possess LVRT capabilities, enabling them to revert to their pre-fault behavior. This is achieved by supplying reactive power to the microgrid during the fault episode. While the PV systems demonstrate the ability to counteract disturbances, they require a “transient recovery time” before complete restoration. This means they cannot instantly revert to their pre-fault behavior immediately following a fault. Upon examining all the subplots, it becomes evident that the EMT simulation offers a more detailed capture of the phenomenon compared to the RMS simulation, which is consistent with expectations. Due to its inherent methodological behavior and finer time-step granularity, the EMT simulation is better equipped to capture high-frequency oscillations accurately. The noticeable overshoots in the EMT simulations further substantiate this claim. Additionally, during the transient period immediately following the fault clearance, the EMT simulation more intricately captures the oscillations induced by the faults and the nonlinear load compared to the RMS simulation. As a result, the transient duration appears more extended in the EMT simulation than in the RMS. A notable limitation of the EMT simulation is its longer completion time than the RMS simulation. However, this difference is minimal in this study due to the compact scale of the microgrid system. In a larger system, this time discrepancy could become more pronounced, potentially affecting the feasibility of using EMT.

### 3.1.2. HVRT Case Scenario

For the HVRT scenario in grid-connected mode, a voltage swell is introduced within the microgrid. This is achieved by incorporating an A.C. voltage source at the busbar (T9), which is proximate to Line\_8\_9, elevating the voltage level to 1.07 p.u. This exceeds the acceptable threshold of 1.05 p.u. This over-voltage condition is initiated at 1 s and remedied by 1.2 s. The overall simulation duration and the time-step increments for both the EMT and RMS simulations remain consistent with previous settings. The behaviors of active power, reactive power, voltage, and current parameters during a voltage swell fault in grid-connected mode are shown in Figure 5.

Active power, reactive power, voltage, and current parameters are plotted separately for this over-voltage fault scenario. It can be observed that the voltage level at Line\_8\_9 rises to 1.07 p.u. due to the voltage swell created at that point. The visible fluctuations in the EMT method during the whole simulation represent the nonlinearity of this system, as there is a large nonlinear load with a THD of 29.4% in the microgrid. The high-frequency overshoots captured by the EMT simulations are the representatives of the faulty behavior of the system. These behaviors go unnoticed in RMS simulation due to its characteristic limitations. However, it is visible in the plot that both the PV systems have HVRT capabilities under grid-connected mode and are able to consume reactive power from the system during voltage swell. They are also capable of keeping the active power very close to the pre-fault value during the over-voltage fault. Similar to the previous scenario, EMT simulations require more time than RMS, but this difference remains inconsequential.



**Figure 5.** Active power, reactive power, voltage, and current behaviors during voltage swell fault in grid-connected mode.

### 3.2. Islanded Mode

In islanded mode operation, the three-phase diesel generator is connected to the microgrid and serves as the reference machine for the system. The same parameters used for the LVRT and HVRT case scenarios in grid-connected mode are also observed in this islanded mode.

#### 3.2.1. LVRT Case Scenario

In the islanded mode's LVRT scenario, a three-phase short-circuit fault was introduced at the same location as in grid-connected mode. The fault was initiated at 1 s and was cleared by 1.2 s. Figure 6 depicts the characteristics of active power, reactive power, voltage, and current parameters during three-phase short-circuit fault in islanded mode.

From the figure, it is evident that the systems possess LVRT capability even in islanded mode. Reactive power was supplied to the system during the short-circuit fault, and the pre-fault values were restored over time. However, distinctions are noticeable between the LVRT scenarios in these two modes. In grid-connected mode, a consistent value was maintained for all parameters during the short-circuit fault, specifically between 1 s and 1.2 s. In islanded mode, there is a noticeable linear decline during the fault, in contrast to the constant value observed in grid-connected mode. This behavior can be attributed to the governor's effect and the AVR system integrated into the generator. Furthermore, in islanded mode, the "transient recovery time" post-fault clearance is more extended compared to the grid-connected scenario. This extended recovery is likely due to the microgrid's dependence on its distributed resources, specifically a standalone diesel generator, resulting in a slower response. As a result, the simulation was extended to 5 s to ensure capturing the return to pre-fault values. The characteristics of RMS and EMT simulations remain the same as before. EMT simulation gave more detailed plots than RMS. However, as the simulations' time length was 5 s, the EMT

simulation needed significantly more time to complete the whole simulation than the grid-connected mode, whereas the RMS simulation took the same amount of time as the grid-connected mode.

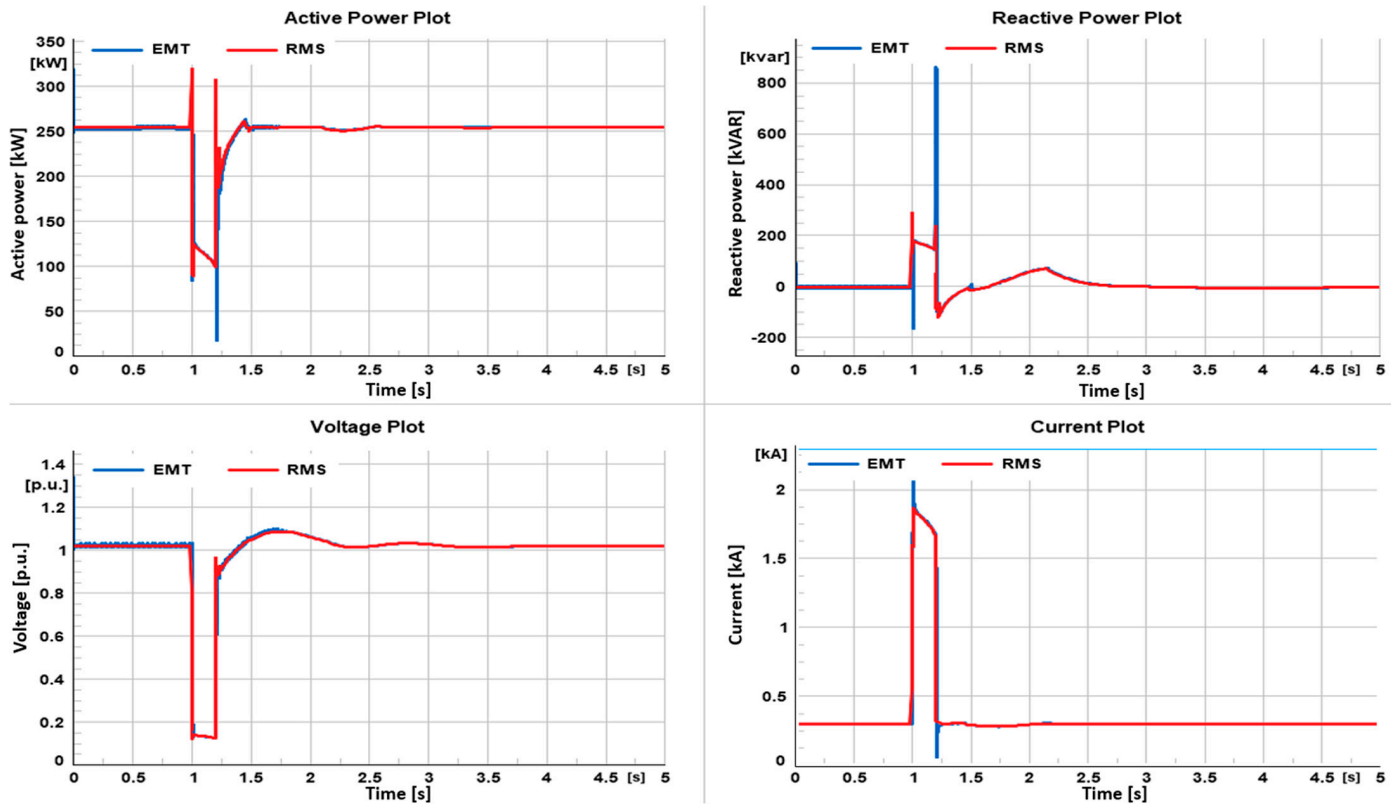


**Figure 6.** Active power, reactive power, voltage, and current behaviors during 3-phase short-circuit fault in islanded mode.

### 3.2.2. HVRT Case Scenario

To evaluate the HVRT capability during islanded mode, a voltage swell was introduced in a manner identical to the previous grid-connected scenario. The swell was initiated at the 1 s mark and persisted for a duration of 200 milliseconds. The behaviors of active power, reactive power, voltage, and current parameters during a voltage swell fault in islanded mode are shown in Figure 7.

Figure 7 illustrates the HVRT capability of the systems while operating in islanded mode. In this scenario, the PV systems actively drew reactive power from the microgrid to offer stabilization during the voltage swell. The transient recovery period in islanded mode was more prolonged than in the grid-connected setting. An important observation to note is that while the active power in grid-connected mode remained closely aligned to its pre-fault values during the disturbance, it showed a significant reduction in this islanded scenario. The difference between RMS and EMT simulation remains as before. The EMT simulation gave more detailed plots than RMS simulation.

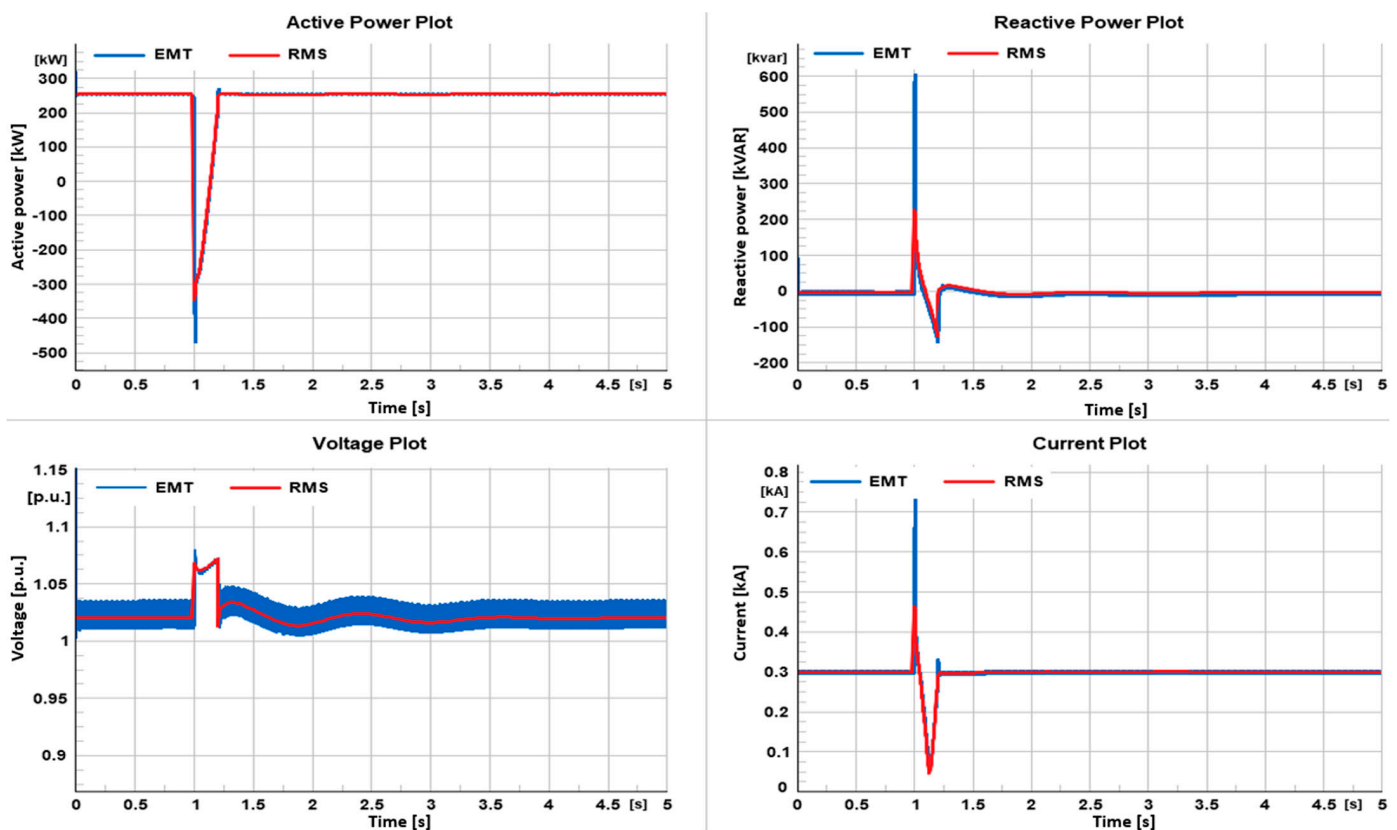


**Figure 7.** Active power, reactive power, voltage, and current behaviors during voltage swell fault in islanded mode.

#### 4. Conclusions

This study presents the transient behaviors of a microgrid in both grid-connected and islanded operations with two PV systems and a nonlinear load. Incorporating PV systems and a diesel generator, this study goes beyond the conventional power-flow studies to scrutinize the system's transient behavior, particularly in the context of LVRT and HVRT events, and assess system resilience in diverse fault scenarios. RMS and EMT simulation techniques yield valuable insights into these complex dynamics. This study reveals several critical findings:

1. The microgrid demonstrates the ability to manage LVRT and HVRT events effectively in both grid-connected and islanded modes.
2. Notable differences exist in the system's transient behavior in grid-connected and islanded modes. In particular, the transient recovery time is longer in islanded mode, attributable to the system's dependence on a single diesel generator for stabilization.
3. While computationally more demanding, EMT simulations provide a more nuanced and detailed understanding of high-frequency transient phenomena, validating their utility for advanced studies. RMS simulations, on the other hand, offer a quicker but less granular insight, affirming their appropriateness for generalized, lower-resolution studies.

The observed variances in transient recovery times between grid-connected and islanded operations point to areas for potential improvement, particularly in optimizing the control strategies for islanded operations.

Overall, this study serves as a comprehensive guide for designing and assessing microgrid systems, especially in environments that require high resiliency and robustness against transient disturbances. In the next stages of our research, we aim to broaden our scope to study microgrids equipped with advanced control systems, ensuring optimal responsiveness and stability even under unpredictable disturbances. Additionally, integrating energy storage solutions, such as BESSes, stands out as a pivotal direction, offering both quick

transient response and enhanced operational flexibility. Beyond these enhancements, we also see value in scaling our analyses to larger, interconnected grid architectures. Such an expansion would provide insights into the nuanced behaviors of expansive power systems, further enriching our understanding of microgrid dynamics in diverse settings.

**Author Contributions:** Conceptualization, A.S.P. and S.S.; methodology, A.S.P. and S.S.; software, A.S.P.; validation, A.S.P. and S.S.; formal analysis, A.S.P. and S.S.; writing—original draft preparation, A.S.P.; writing—review and editing, S.S.; visualization, A.S.P.; supervision, S.S.; project administration, S.S.; funding acquisition, S.S. All authors have read and agreed to the published version of the manuscript.

**Funding:** This research was funded by the U.S. Department of Energy Office of Energy Efficiency and Renewable Energy, Solar Energy Technology Office through Established Program to Stimulate Competitive Research (EPSCoR) Program under Grant DE-SC0020281. The views expressed in the article do not necessarily represent the views of the DOE.

**Institutional Review Board Statement:** Not applicable.

**Informed Consent Statement:** Not applicable.

**Conflicts of Interest:** The authors declare no conflict of interest.

## References

1. Lopes, J.A.P.; Hatziargyriou, N.; Mutale, J.; Djapic, P.; Jenkins, N. Integrating Distributed Generation into Electric Power Systems: A Review of Drivers, Challenges and Opportunities. *Electr. Power Syst. Res.* **2007**, *77*, 1189–1203. [CrossRef]
2. Venkataramanan, G.; Marnay, C. A Larger Role for Microgrids. *IEEE Power Energy Mag.* **2008**, *6*, 78–82. [CrossRef]
3. REN21. Renewables 2022 Global Status Report. Available online: <https://www.ren21.net/gsr-2022> (accessed on 29 August 2023).
4. Lidula, N.W.A.; Rajapakse, A.D. Microgrids Research: A Review of Experimental Microgrids and Test Systems. *Renew. Sustain. Energy Rev.* **2011**, *15*, 186–202. [CrossRef]
5. Katiraei, F.; Iravani, R.; Hatziargyriou, N.; Dimeas, A. Microgrids Management. *IEEE Power Energy Mag.* **2008**, *6*, 54–65. [CrossRef]
6. Sepasi, S.; Toledo, S.; Kobayashi, J.; Roose, L.R.; Matsuura, M.M.; Tran, Q.T. A Practical Solution for Excess Energy Management in a Diesel-Backed Microgrid with High Renewable Penetration. *Renew. Energy* **2023**, *202*, 581–588. [CrossRef]
7. Reihani, E.; Sepasi, S.; Roose, L.R.; Matsuura, M. Energy Management at the Distribution Grid Using a Battery Energy Storage System (BESS). *Int. J. Electr. Power Energy Syst.* **2016**, *77*, 337–344. [CrossRef]
8. Nasri, M.; Hossain, M.R.; Ginn, H.L.; Moallem, M. Distributed Control of Converters in a DC Microgrid Using Agent Technology. In Proceedings of the 2016 Clemson University Power Systems Conference (PSC), Clemson, SC, USA, 8–11 March 2016; pp. 1–6.
9. Sarfi, V.; Niaazari, I.; Livani, H. Multiobjective Fireworks Optimization Framework for Economic Emission Dispatch in Microgrids. In Proceedings of the 2016 North American Power Symposium (NAPS), Denver, CO, USA, 18–20 September 2016; pp. 1–6.
10. Tran, Q.T.; Davies, K.; Sepasi, S. Isolation Microgrid Design for Remote Areas with the Integration of Renewable Energy: A Case Study of Con Dao Island in Vietnam. *Clean Technol.* **2021**, *3*, 804–820. [CrossRef]
11. Foruzan, E.; Algrain, M.C.; Asgarpoor, S. Low-Voltage Ride-through Simulation for Microgrid Systems. In Proceedings of the 2017 IEEE International Conference on Electro Information Technology (EIT), Lincoln, NE, USA, 14–17 May 2017; pp. 260–264.
12. Davies, K.L.; Tran, T.; Sepasi, S.; Roose, L.R. Distribution Grid Monitoring. U.S. Patent No. 11,146,103, 12 October 2021.
13. Truong, D.-N.; Thi, M.-S.N.; Le, H.-G.; Do, V.-D.; Ngo, V.-T.; Hoang, A.-Q. Dynamic Stability Improvement Issues with a Grid-Connected Microgrid System. In Proceedings of the 2019 International Conference on System Science and Engineering (ICSSE), Dong Hoi, Vietnam, 20–21 July 2019; pp. 214–218.
14. Niranjana, P.; Gupta, P.K.; Ahmad, P.; Choudhary, N.K.; Singh, N.; Singh, R.K. Protection Coordination Scheme in Microgrid with Common Optimal Settings of User-Defined Dual-Setting Overcurrent Relays. In Proceedings of the 2023 5th International Conference on Energy, Power and Environment: Towards Flexible Green Energy Technologies (ICEPE), Shillong, India, 15–17 June 2023; pp. 1–5.
15. Sepasi, S.; Talichet, C.; Pramanik, A.S. Power Quality in Microgrids: A Critical Review of Fundamentals, Standards, and Case Studies. *IEEE Access* **2023**, *11*, 108493–108531. [CrossRef]
16. Machowski, J.; Lubosny, Z.; Bialek, J.W.; Bumby, J.R. *Power System Dynamics: Stability and Control*, 3rd ed.; Wiley: Hoboken, NJ, USA, 2020. Available online: <https://www.wiley.com/en-us/power+system+dynamics%3a+stability+and+control%2c+3rd+edition-p-9781119526360> (accessed on 29 August 2023).
17. Cigré; CIRED. *Modelling of Inverter-Based Generation for Power System Dynamic Studies*; Conseil International des Grands Réseaux Électriques, Congrès International des Réseaux Électriques de Distribution, Eds.; CIGRÉ: Paris, France, 2018; ISBN 978-2-85873-429-0.
18. Favuzza, S.; Musca, R.; Zizzo, G. A Comparison between RMS and EMT Grid-Forming Implementations in MATLAB/Simscap for Smart Grids Dynamics. In Proceedings of the 2022 IEEE 21st Mediterranean Electrotechnical Conference (MELECON), Palermo, Italy, 14–16 June 2022; pp. 1079–1084.

19. Acosta, M.A.C.; Soares, B.M.M.; Abildgaard, H.; Parrini, D.R.; Shattuck, A.; Da Costa, I.C.; da Rosa, T. Wind Power Plant Modelling Benchmark of RMS vs EMT Simulation Models for the Electric Reliability Council of Texas (ERCOT) Market. In Proceedings of the 20th International Workshop on Large-Scale Integration of Wind Power into Power Systems as well as on Transmission Networks for Offshore Wind Power Plants (WIW 2021), Online, 29–30 September 2021; Volume 2021, pp. 503–508.
20. Subedi, S.; Rauniyar, M.; Ishaq, S.; Hansen, T.M.; Tonkoski, R.; Shirazi, M.; Wies, R.; Cicilio, P. Review of Methods to Accelerate Electromagnetic Transient Simulation of Power Systems. *IEEE Access* **2021**, *9*, 89714–89731. [[CrossRef](#)]
21. Teodorescu, R.; Liserre, M.; Rodriguez, P. *Grid Converters for Photovoltaic and Wind Power Systems*; IEEE eBooks; Wiley-IEEE Press: Hoboken, NJ, USA, 2007. Available online: <https://ieeexplore.ieee.org/book/5732788> (accessed on 29 August 2023).
22. Clark, A.; Mitra, P.; Johansson, N.; Ghandhari, M. Development of a Base Model in RMS and EMT Environment to Study Low Inertia System. In Proceedings of the 2021 IEEE Power & Energy Society General Meeting (PESGM), Washington, DC, USA, 25–29 July 2021; pp. 1–5.
23. Liu, P.; Zhu, G.; Ding, L.; Gao, X.; Jia, C.; Ng, C.; Terzija, V. High-Voltage Ride-through Strategy for Wind Turbine with Fully-Rated Converter Based on Current Operating Range. *Int. J. Electr. Power Energy Syst.* **2022**, *141*, 108101. [[CrossRef](#)]
24. Jayawardena, A.V. Contributions to the Development of Microgrids: Aggregated Modelling and Operational Aspects. Ph.D. Thesis, University of Wollongong, Wollongong, NSW, Australia, 2015.
25. Safaei, A.; Hosseini, S.H.; Abyaneh, H.A. Enhancing the HVRT and LVRT Capabilities of DFIG-Based Wind Turbine in an Islanded Microgrid. *Eng. Technol. Appl. Sci. Res.* **2017**, *7*, 2118–2123. [[CrossRef](#)]
26. Steinhäuser, L.; Coumont, M.; Weck, S.; Hanson, J. Comparison of RMS and EMT Models of Converter-Interfaced Distributed Generation Units Regarding Analysis of Short-Term Voltage Stability. In Proceedings of the NEIS 2019 Conference on Sustainable Energy Supply and Energy Storage Systems, Hamburg, Germany, 19–20 September 2019; pp. 1–6.
27. Conti, S.; Greco, A.M.; Messina, N.; Vagliasindi, U. Intentional Islanding of MV Microgrids: Discussion of a Case Study and Analysis of Simulation Results. In Proceedings of the Automation and Motion 2008 International Symposium on Power Electronics, Electrical Drives, Ischia, Italy, 11–13 June 2008; pp. 422–427.
28. Perumal, P.; Ramasamy, A.K.; Teng, A.M. Performance Analysis of the DigSILENT PV Model Connected to a Modelled Malaysian Distribution Network. *IJCA* **2016**, *9*, 75–88. [[CrossRef](#)]
29. Arraño-Vargas, F.; Konstantinou, G. Development of Real-Time Benchmark Models for Integration Studies of Advanced Energy Conversion Systems. *IEEE Trans. Energy Convers.* **2020**, *35*, 497–507. [[CrossRef](#)]
30. Yap, K.Y.; Lim, J.M.-Y.; Sarimuthu, C.R. A Novel Adaptive Virtual Inertia Control Strategy under Varying Irradiance and Temperature in Grid-Connected Solar Power System. *Int. J. Electr. Power Energy Syst.* **2021**, *132*, 107180. [[CrossRef](#)]
31. Li, F.; Liu, M.; Wang, Y.; Zhang, X. Research on HIL-Based HVRT and LVRT Automated Test System for Photovoltaic Inverters. *Energy Rep.* **2021**, *7*, 405–412. [[CrossRef](#)]
32. D. GmbH. *DIgSILENT PowerFactory 2022 MV Microgrid Model*; DIgSILENT: Gomaringen, Germany, 2022.
33. D. GmbH. *DIgSILENT PowerFactory 2022 User Manual*; DIgSILENT: Gomaringen, Germany, 2022.
34. D. GmbH. *DIgSILENT PowerFactory 2022 Technical Reference for General Load Model*; DIgSILENT: Gomaringen, Germany, 2022.
35. D. GmbH. *DIgSILENT PowerFactory 2022 Technical Reference for 3-Phase, 2-Windings Transformer Models*; DIgSILENT: Gomaringen, Germany, 2022.
36. D. GmbH. *DIgSILENT PowerFactory 2022 Technical Reference for Power Measurement*; DIgSILENT: Gomaringen, Germany, 2022.
37. D. GmbH. *DIgSILENT PowerFactory 2022 Technical Reference for Voltage Measurement*; DIgSILENT: Gomaringen, Germany, 2022.
38. D. GmbH. *DIgSILENT PowerFactory 2022 Technical Reference for Phase Measurement*; DIgSILENT: Gomaringen, Germany, 2022.
39. D. GmbH. *DIgSILENT PowerFactory 2022 Technical Reference for Static Generator*; DIgSILENT: Gomaringen, Germany, 2022.
40. D. GmbH. *DIgSILENT PowerFactory 2022 Technical Reference for Synchronous Machine Models*; DIgSILENT: Gomaringen, Germany, 2022.
41. D. GmbH. *DIgSILENT PowerFactory 2022 Technical Reference for External Grid*; DIgSILENT: Gomaringen, Germany, 2022.

**Disclaimer/Publisher’s Note:** The statements, opinions and data contained in all publications are solely those of the individual author(s) and contributor(s) and not of MDPI and/or the editor(s). MDPI and/or the editor(s) disclaim responsibility for any injury to people or property resulting from any ideas, methods, instructions or products referred to in the content.